Supplemental Material: Emergence of spinons in layered trimer iridate $Ba_4Ir_3O_{10}$

(Dated: October 15, 2022)

This document provides methods information, the bond valence sum analysis, additional details of the X-ray measurements, and description of the lineshape fitting.

METHODS

Single crystals of $Ba_4Ir_3O_{10}$ were grown using the flux method as described in Ref. [1]. The resonant inelastic x-ray scattering (RIXS) experiments were performed at the 27-ID-B station of the Advanced Photon Source at Argonne National Laboratory. All RIXS data were collected at the Ir L_3-edge with a horizontal scattering plane and π polarization. Wavevectors throughout the manuscript are defined using standard reciprocal lattice units (r.l.u.) notation as $\boldsymbol{Q}= H\mathbf{a}^* + K\mathbf{b}^* + L\mathbf{c}^*$ based on lattice constants a =7.2545 Å, b =13.192 Å, c =5.7737 Å, $\alpha = \gamma = 90°$, β = 113.513° and space group $P2_1/c$ (No. 14). The energy resolution was around 32 meV. The resonant elastic x-ray scattering (REXS) measurements were carried out at the Coherent Soft X-Ray (CSX) 23-ID-1 beamline at the National Synchrotron Light Source II with x-ray energy tuned to the O K-edge, π x-ray polarization and a vertical scattering geometry. Due to the spin-orbit coupling (SOC) of Ir and hybridization between Ir and O, O K-edge REXS is sensitive to magnetic order in iridates [2]. Meanwhile, the small penetration depth and long wavelength of O K-edge x-rays help suppress multi scattering events which can present a challenge in Ir L_3-edge REXS experiments.

BOND VALENCE SUM ANALYSIS

The bond valence sum is a widely utilized means to estimate the oxidation states of atoms in a compound. Here we use it to test the possibility of intra-trimer charge disproportionation in $Ba_4Ir_3O_{10}$. The valence V of an atom can be evaluated by summing up the individual bond valences v_i surrounding the atom, which have a simple relationship with the bond lengths [3]:

$$V = \sum_i v_i = \sum_i \exp(\frac{R_o - R_i}{B}) \tag{1}$$

where B = 0.37 Å is an empirical constant, R_i is the bond length in the target material, and R_0 is the reference bond length for an element of exact valence, for which we use tabulated values of 1.87 Å, derived for Ir^{4+}-O^{2-} bonds [4]. We use the $Ba_4Ir_3O_{10}$ structure reported in Ref. [1]. The corresponding valence is 4.16+ and 3.87+ for Ir1 and Ir2, respectively, indicating that charge disproportionation is small and of minimal importance for the physics discuss here. It is certainly far too small to generate an effectively spinless central iridium atom, as has been proposed for Ru based material $Ba_4Ru_3O_{10}$ [5]. We note that inter-trimer disproportionation is forbidden since the trimers are symmetrically equivalent in $Ba_4Ir_3O_{10}$.

FITTING OF THE REXS DATA

For the REXS measurements, we used a piece of $(Ba_{1-x}Sr_x)_4Ir_3O_{10}$ (x =0.02) single crystal with a surface normal of [H, 0, 0]. We put the [H, 0, 0] and [0, 0, L] directions in the vertical scattering plane and used π incident x-ray polarization. The Coherent Soft X-Ray (CSX) 23-ID-1 beamline at the National Synchrotron Light Source II has a fast CCD detector with 30×30 μm^2 pixels placed 340 mm from the sample. At 25 K, a well-defined peak emerged in the fast CCD image [Fig. S1(a)], corresponding to the superlattice peak at $\boldsymbol{Q}$=(0.5, 0, 0). The speckle pattern arises from the interference of the coherent x-ray beam scattered by different magnetic domains [6]. The peak intensity is extracted by summing up the pixel readings in the region of interest that is marked by the dashed rectangle in Fig. S1(a). Figure S1(b) shows the incident energy dependence of the peak intensity at fixed $\boldsymbol{Q}$=(0.5, 0, 0) in which resonant behavior can be observed. The multiple resonant peaks may be caused by the symmetry-distinct oxygen sites that have different binding energies. By comparing the theta-2theta scans at the non-resonant (524 eV) and resonant (527 eV) energies [Fig. S1(c)-(p)], we find two different contributions to the signals. One is a tiny peak that is independent of incident energy or temperature (gray shaded areas), which comes from the second harmonic of the

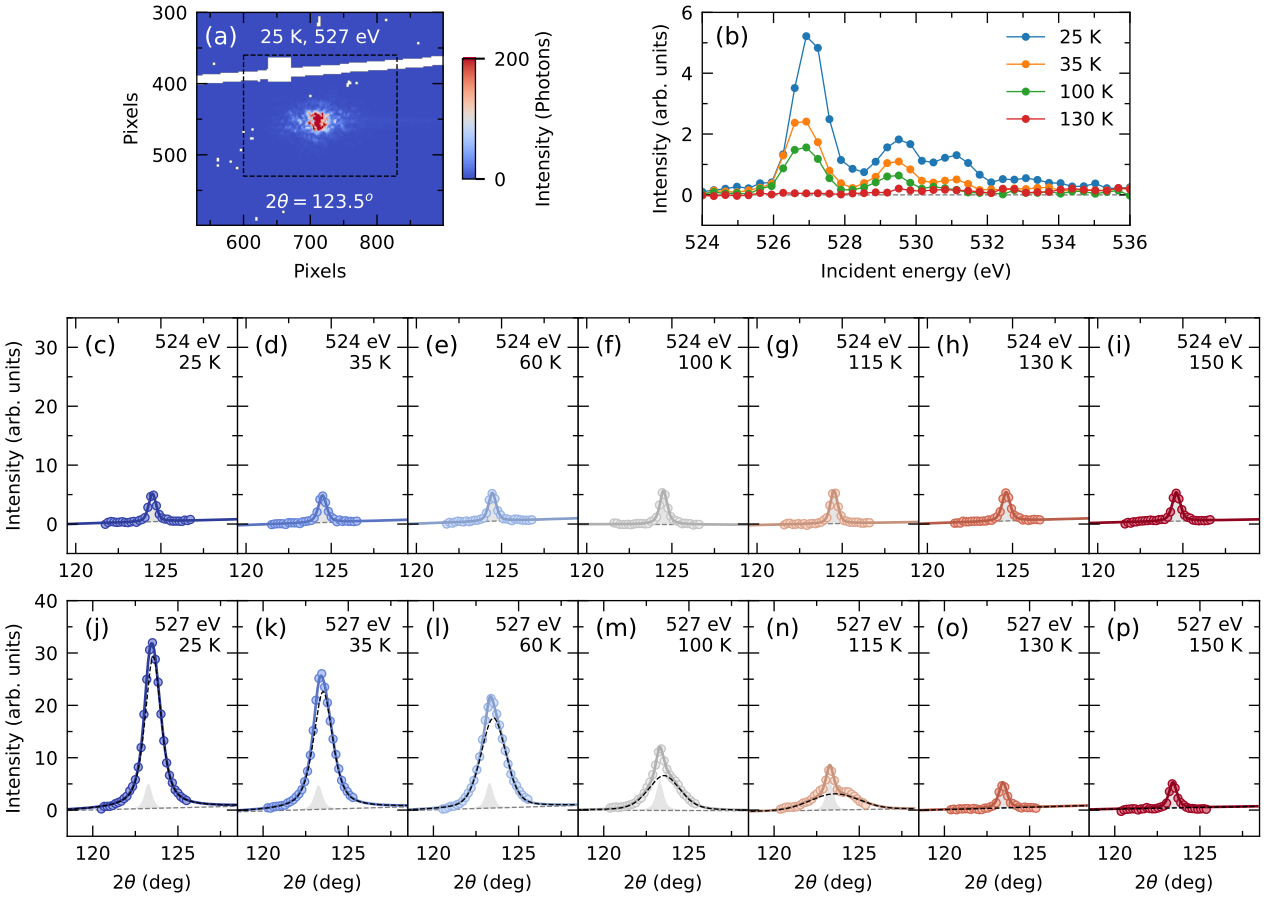

FIG. S1. Fitting of the REXS data at O K-edge. (a) A representative detector image of the superlattice peak at $\boldsymbol{Q}$=(0.5, 0, 0). The dashed lines envelop the region of interest in which the pixel readings are summed up to extract the peak intensity. The white pixels originate from the beamstop/detector errors that have been removed from the data. (b) Incident energy dependence of the superlattice peak intensity at different temperatures. The small energy shift ($<$ 0.3 eV) between the energy scans of different temperature is due to the photon energy change associated with the monochromator that is sensitive to thermal perturbations. (c)-(p) A series of theta-2theta scans with different incident energy and temperature. The circles are the data and the solid lines are the fitting results which can be further broken into several components including a sloped background (gray dashed lines), a pseudo-Voigt function presenting the second harmonic of the Bragg peak (gray shaded area) and another pseudo-Voigt function outlining the magnetic contributions (black dashed lines).

(1, 0, 0) Bragg peak. Another contribution shows clear resonant behavior (black dashed lines), indicating a magnetic origin. It weakens with increasing temperature and disappears above 130 K, consistent with previously reported magnetic transition [1]. The pure magnetic contribution can be isolated by fitting the theta-2theta scan with a sloped background and two pseudo-Voigt profiles, the results of which are shown in Fig. 3(a), (b) of the main text.

FITTING OF THE RIXS SPECTRA

As shown in Fig. 1(b), a representative RIXS spectrum is composed of a quasi-elastic line, low-energy magnetic excitations and high-energy *dd*-excitations. A constant background has been subtracted for all the spectra using the energy-gain side. The quasi-elastic peak includes the elastic line and potential phonon excitations which turn out to be negligible. Thus, we fit the quasi-elastic peak with a pseudo-Voigt profile that is primarily determined by the energy resolution. The lineshape of the magnetic excitations can be adequately captured phenomenologically by a damped harmonic oscillator convoluted with the resolution. In Fig. 1(b) of the main text, the *dd* excitations are fitted with multiple pseudo-Voigt functions. For Fig. 2 and Fig. 3, the *dd* excitations are not fully covered during the measurements, so we use an error function to account for the tail of *dd*-excitations for simplicity. The fitting

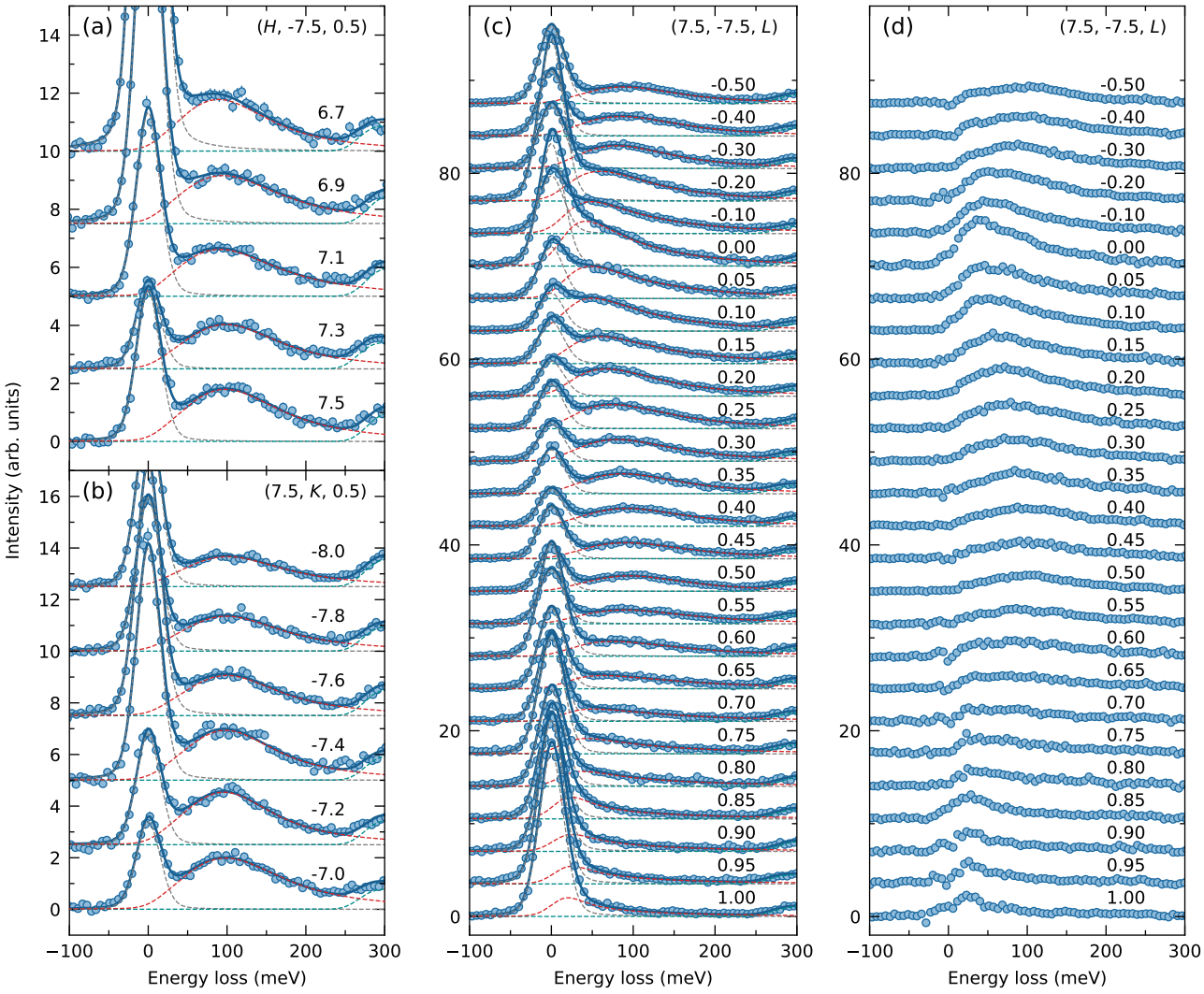

FIG. S2. Fitting of the Ir L_3-edge RIXS data in undoped $Ba_4Ir_3O_{10}$ collected at 8 K. (a)-(c) Background subtracted RIXS spectra at different $\boldsymbol{Q}$ points. The circles present the data and the dashed lines of different colors are fittings of different components, the summation of which leads to the solid lines. (d) RIXS spectra with the quasi-elastic line and *dd*-excitations subtracted. The same set of data produces Fig. 2(c) in the main text.

results are plotted in Fig. S2(a)-(c) and Fig. S3(a)-(c). After subtracting the quasi-elastic line and *dd*-excitations, the magnetic excitations are well isolated, which are presented in Fig. 2(a)-(c), Fig. 3(c)-(e), Fig. S2(d), and Fig. S3(d). The extracted dispersion along the L direction is plotted in Fig. S4, in which the energy positions of intensity maxima from fits are used since the harmonic oscillator is overdamped near the zone center.

DETAILS OF THE CLUSTER EXACT DIAGONALIZATION CALCULATIONS

To help understand the strong coupling model, we perform cluster exact diagonalization (ED) calculations using the EDRIXS software [7]. A three-Ir-site cluster is constructed as shown in Fig. S5. We explicitly include the onsite Coulomb interactions and spin orbital couplings in the Hamiltonian. Based on the short Ir-Ir bond distances and the close-to-right-angle Ir-O-Ir bonds, the leading interactions between the Ir atoms are expected to be direct hopping, so we proceed based on the same approach as that used in Ref. 8 and implement inter-atomic *d*-*d* hopping integrals between the $5d$ orbitals of the neighbored Ir sites using the Slater-Koster method. The interactions are first implemented in the trigonal notation (global coordinates) and are transformed into octahedral notation (local coordinates) subsequently. Regarding the orbital basis, we consider $t_{2g}^{15}e_g^0$ and $t_{2g}^{14}e_g^1$ configurations as the double e_g

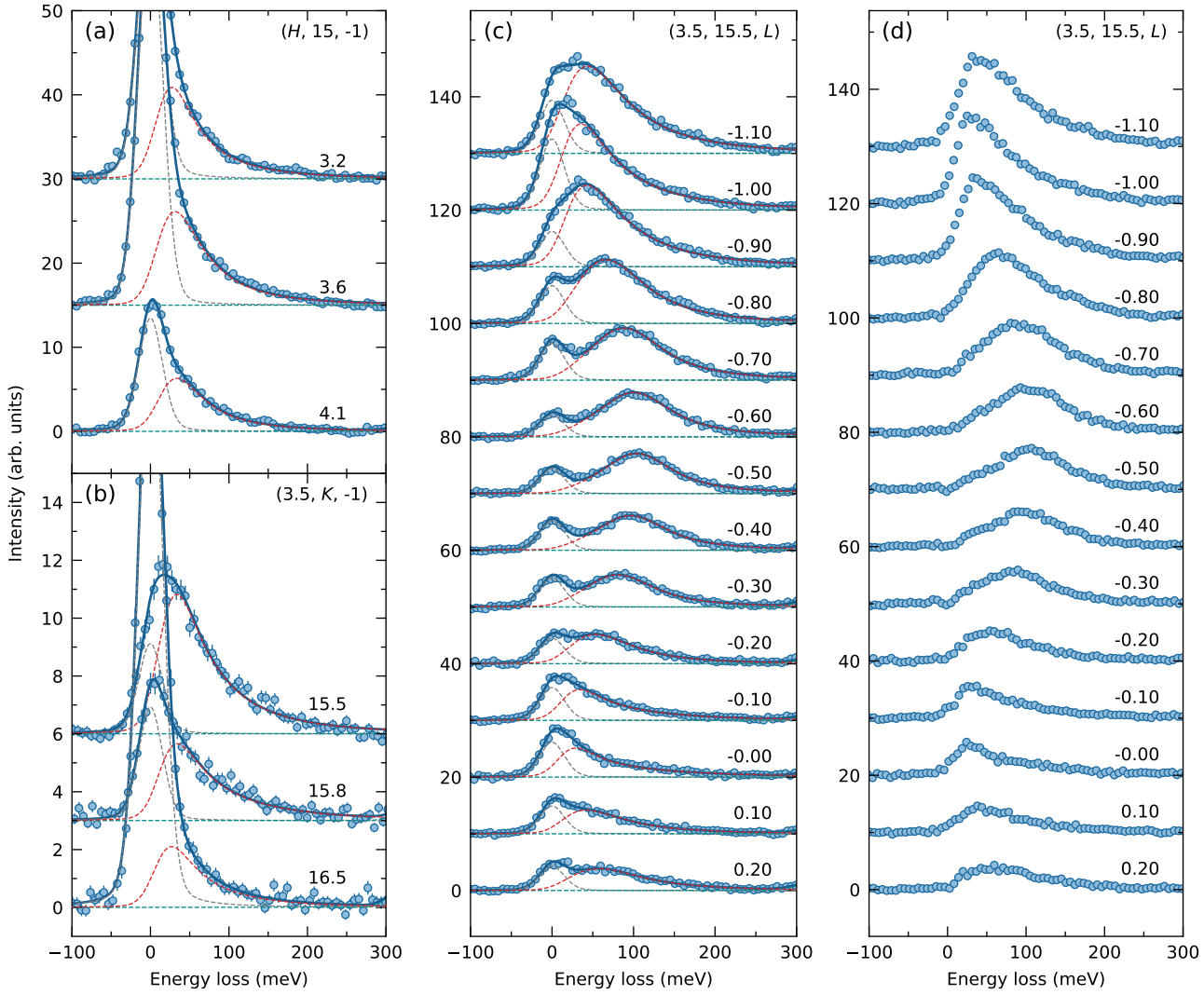

FIG. S3. Fitting of the Ir L_3-edge RIXS data in doped $(Ba_{1-x}Sr_x)_4Ir_3O_{10}$ ($x = 0.02$) collected at 8 K. (a)-(c) Background subtracted RIXS spectra along with fitting results presented by dashed lines of different colors. (d) RIXS spectra with the quasi-elastic line and *dd*-excitations subtracted. The same set of data produces Fig. 3(c) in the main text.

occupancy is minimal. The full set of parameters used for the ED calculations is listed in Table S1.

As mentioned in the main text, in the absence of inter-Ir-site hopping, the ground state for each Ir site with a nominal $5d^5$ configuration is an $S_{\text{eff}} = 1/2$ doublet. With finite inter-Ir-site hopping, the three doublets from the three Ir sites will recombined and split into several multiplets. For the antisymmetric doublet $|S = 1/2\rangle^-$, the two Ir sites at the edge of the trimer form a singlet and the spin of the middle Ir site remains free. In the symmetric doublet $|S = 1/2\rangle^+$, the two Ir sites at the edge form a triplet which keeps antiparallel to the middle Ir site spin. These two doublets are protected by symmetry. An additional high-spin multiplet $|S = 3/2\rangle$ lies at higher energy than these two doublets given the antiferromagnetic interactions, the degeneracy of which is lifted by anisotropic interactions, making it split into $|S = 3/2, S_z = \pm 1/2\rangle$ and $|S = 3/2, S_z = \pm 3/2\rangle$ doublets. The transitions between $|S = 1/2\rangle^-$ and $|S = 1/2\rangle^+$ doublets contribute to the magnetic signals below 0.25 eV while the transitions to $|S = 3/2\rangle$ multiplets are indicated by the peak at ∼0.35 eV in Fig. 1(b). As shown in the main text, the competition among intra-trimer interactions leads to a critical point where the $|S = 1/2\rangle^-$ and $|S = 1/2\rangle^+$ doublets become degenerate. The exact position of the critical point depends on both the Coulomb interactions and spin orbital coupling.

The presence of the critical point is a consequence of the competition between J_1 and J_3. Indeed, in a mean-field level, $|S = 1/2\rangle^+$ and $|S = 1/2\rangle^-$ becomes degenerate when $J_1 = J_3$ in the isotropic case [9]. This form of calculation between the interactions can explain both the emergent 1D behavior in $Ba_4Ir_3O_{10}$ and the fragility of the quantum

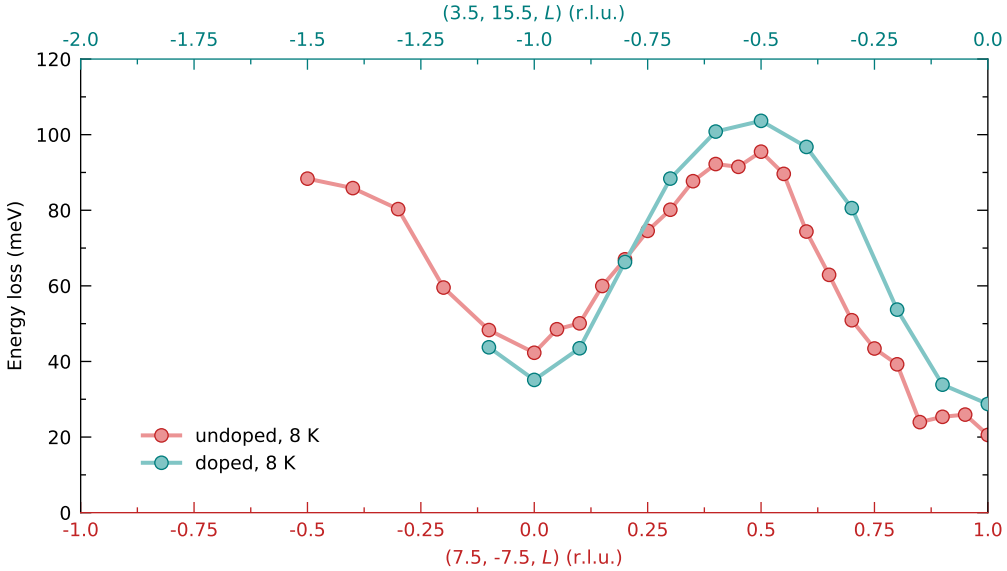

FIG. S4. Energy positions of magnetic excitation maxima as a function of L for undoped $Ba_4Ir_3O_{10}$ and doped $(Ba_{1-x}Sr_x)_4Ir_3O_{10}$ ($x = 0.02$).

TABLE S1. Full list of parameters used for the ED calculations. Here, we only consider the cubic crystal field splitting and fix $V_{dd\sigma} = -2.3V_{dd\pi}$, $V_{dd\pi} = 1.3V_{dd\delta}$ [10]. F^0_{dd}, F^0_{dd} and F^0_{dd} are Slater integrals for the Ir 5d orbitals and is the spin orbital coupling strength. All parameters are in units of eV.

$10D_q$	F^0_{dd}	F^2_{dd}	F^4_{dd}	
3.5	2.66	2.58	1.62	0.33

spin liquid (QSL) state in $(Ba_{1-x}Sr_x)_4Ir_3O_{10}$. Upon doping, the system is slightly driven away from the critical point, making the spinons more confined. Considering that the changes of lattice parameters and atomic coordinates on doping are minimal [1], the modification of the exchange interactions is expected to be subtle which can be driven by either the change of inter-site hopping or the screening of Coulomb interactions caused by the surrounding oxygens. Thus, the intra-chain interactions, both $J_{\rm chain}$ and Δ, would be largely preserved, which is consistent with the observation that the overall dispersion along L direction remains quite similar in the doped sample [Fig. 2(c) and Fig. 3(c) in the main text].

ADDITIONAL CALCULATIONS OF THE SPINON CONTINUUM

In Fig. 2(c) of the main text, we show the excitation boundaries of the spinon continuum. Here, we present more results about the spinon excitation calculations. The calculated spinon continuum spectrum is shown in Fig. S6(a), using the same parameters as in the main text. Our effective model further captures the energy-width and boundaries of the continuum, but only approximates the detailed lineshape. This could arise from further sub-leading exchange interactions in the full magnetic Hamiltonian for $Ba_4Ir_3O_{10}$, such as the off-diagonal terms, which could come into play given the strong SOC and low structural symmetry of $Ba_4Ir_3O_{10}$. Note that the contributions from higher order four-spinon excitations fade rapidly with increasing Δ [11].

Moreover, the spinon continuum we calculated here only involves the zigzag chains formed by the Ir sites at the edge of the trimers. The presence of the middle Ir sites is expected to provide extra correlations, making the lineshape deviate from a simple picture of an antiferromagnetic spin chain. To test with a more realistic model and further explore the effect of exchange anisotropy on spinon excitations, we performed additional density matrix renormalization group (DMRG) calculations within the strong coupling regime using the same model as described in

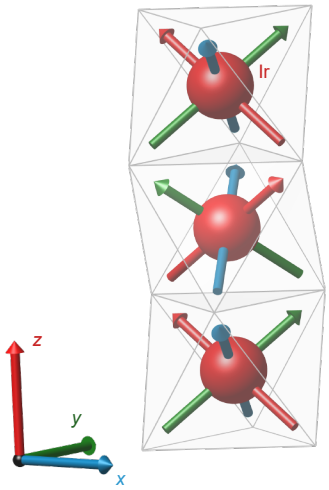

FIG. S5. Illustration of the cluster model used in the ED calculations. Both the global Cartesian coordinates defined in the trigonal notation and the local coordinates defined in the octehedral notation are presented with the same color coding.

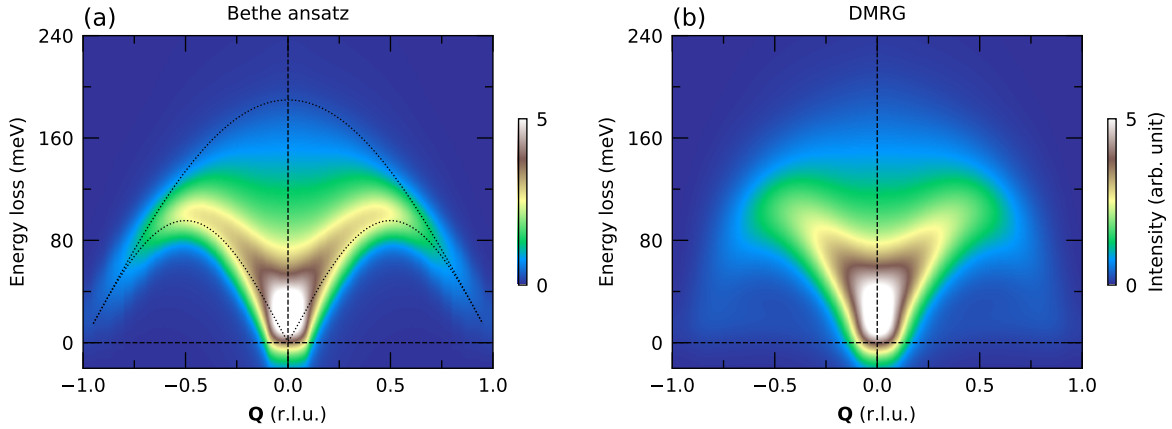

FIG. S6. Calculated spinon excitations along the chain direction. (a) Two-spinon dynamical structure factor of an antiferromagnetic spin-1/2 chain calculated using Bethe ansatz with $J_{\text{chain}} = 55$ meV and $\Delta = 1.3$. The dotted lines are the calculated excitation boundaries without broadening. (b) Dynamical structure factor calculated using DMRG approach as described in Ref. 9 with $J_1^{xx} = 181.5$, $J_2^{xx} = 45.375$, $J_3^{xx} = 195.1125$ meV and $\Delta = 2$. Only the contributions from the Ir atoms within the chains are presented. The spectra in both panels are convoluted with instrument resolution function and the dashed lines are guides to the eye.

Ref. 9, which demonstrates the intra-trimer frustration in the isotropic limit. With $\Delta > 1$, since the transformation of $S_z \rightarrow -S_z$ leaves the Hamiltonian invariant, the low-energy multiplet still represents two $S = 1/2$ multiplets, $|S = 1/2\rangle^-$ and $|S = 1/2\rangle^+$, that cross in a linear fashion when tuning J_1 across J_3. Consequently, the calculated spectrum is qualitatively the same as in the isotropic case. Figure S6(b) shows the results with $\Delta = 2$, which is larger than the value determined from RIXS data in order to enhance the spin gap. It turns out that the spin gap is rather small despite a very sizeable Δ. The calculated spectrum shows robustly a spinon continuum but with a modified lineshape.

Overall, the current minimal model turns out to be a good description of the most important interactions in $Ba_4Ir_3O_{10}$.

[1] Gang Cao, Hao Zheng, Hengdi Zhao, Yifei Ni, Christopher A. Pocs, Yu Zhang, Feng Ye, Christina Hoffmann, Xiaoping Wang, Minhyea Lee, Michael Hermele, and Itamar Kimchi, "Quantum liquid from strange frustration in the trimer magnet $Ba_4Ir_3O_{10}$," npj Quantum Materials **5**, 26 (2020).

[2] X. Liu, M. P. M. Dean, J. Liu, S. G. Chiuzbăian, N. Jaouen, A. Nicolaou, W. G. Yin, C. Rayan Serrao, R. Ramesh, and H. Ding, "Probing single magnon excitations in Sr_2IrO_4 using O K-edge resonant inelastic x-ray scattering," Journal of Physics: Condensed Matter **27**, 202202 (2015).

[3] David I. Brown, *The Chemical Bond in Inorganic Chemistry: The Bond Valence Model* (Oxford University Press, 2006).

[4] "Bond valence parameters," https://www.iucr.org/resources/data/data-sets/bond-valence-parameters, accessed: 2021-11-15.

[5] S. V. Streltsov and D. I. Khomskii, "Unconventional magnetism as a consequence of the charge disproportionation and the molecular orbital formation in $Ba_4Ru_3O_{10}$," Physical Review B **86**, 064429 (2012).

[6] Y. Shen, G. Fabbris, H. Miao, Y. Cao, D. Meyers, D. G. Mazzone, T. A. Assefa, X. M. Chen, K. Kisslinger, D. Prabhakaran, A. T. Boothroyd, J. M. Tranquada, W. Hu, A. M. Barbour, S. B. Wilkins, C. Mazzoli, I. K. Robinson, and M. P. M. Dean, "Charge condensation and lattice coupling drives stripe formation in nickelates," Physical Review Letters **126**, 177601 (2021).

[7] "EDRIXS website," https://github.com/NSLS-II/edrixs, accessed: 2021-09-27.

[8] K. I. Kugel, D. I. Khomskii, A. O. Sboychakov, and S. V. Streltsov, "Spin-orbital interaction for face-sharing octahedra: Realization of a highly symmetric SU(4) model," Physical Review B **91**, 155125 (2015).

[9] Andreas Weichselbaum, Weiguo Yin, and Alexei M. Tsvelik, "Dimerization and spin decoupling in a two-leg Heisenberg ladder with frustrated trimer rungs," Physical Review B **103**, 125120 (2021).

[10] O. K. Andersen, W. Klose, and H. Nohl, "Electronic structure of Chevrel-phase high-critical-field superconductors," Physical Review B **17**, 1209–1237 (1978).

[11] Isaac Pérez Castillo, "The exact two-spinon longitudinal dynamical structure factor of the anisotropic XXZ model," arXiv e-prints , arXiv:2005.10729 (2020).